

## Photocatalytic properties of the g-C<sub>3</sub>N<sub>4</sub>/\{010\} facets BiVO<sub>4</sub> interface Z-Scheme photocatalysts induced by BiVO<sub>4</sub> surface heterojunction



Ying Wang<sup>a</sup>, Guoqiang Tan<sup>a,\*</sup>, Ting Liu<sup>a</sup>, Yuning Su<sup>a</sup>, Huijun Ren<sup>b</sup>, XinLei Zhang<sup>a</sup>, Ao Xia<sup>a</sup>, Long Lv<sup>c</sup>, Yun Liu<sup>d</sup>

<sup>a</sup> School of Materials Science and Engineering, Shaanxi University of Science & Technology, Xi'an, 710021, China

<sup>b</sup> School of Arts and Sciences, Shaanxi University of Science & Technology, Xi'an, 710021, China

<sup>c</sup> Department of Information Engineering, Engineering University of PAP, Xi'an, 710086, China

<sup>d</sup> College of Electrical and Information Engineering, Shaanxi University of Science & Technology, Xi'an, 710021, China

### ARTICLE INFO

**Keywords:**  
BiVO<sub>4</sub> surface heterojunction  
g-C<sub>3</sub>N<sub>4</sub>  
Interface Z-scheme heterojunction  
Built-in electric field

### ABSTRACT

The g-C<sub>3</sub>N<sub>4</sub>/\{010\} facets BiVO<sub>4</sub> interface Z-scheme photocatalysts is fabricated by ultrasonic dispersion method. The density functional theory (DFT) shows that the differences of the energy levels in the conduction bands and the valence bands between the \{010\} and \{110\} facets of BiVO<sub>4</sub> is about 0.37 and 0.31 V (vs. NHE, pH = 7), respectively. Therefore, the co-exposed \{010\} and \{110\} facets of BiVO<sub>4</sub> can form surface heterojunction, which promotes the \{010\} facets of BiVO<sub>4</sub> with negative charge. The zeta potential indicates that layered g-C<sub>3</sub>N<sub>4</sub> with positive charge. The Raman, FT-IR and XPS analysis demonstrates that the layered g-C<sub>3</sub>N<sub>4</sub> is anchored on the \{010\} facets of BiVO<sub>4</sub> through strong interface electrostatic interaction, which leads to form a built-in electric field at the contact interface. Under the built-in electric field driving, photogenerated electrons in the CB of \{010\} facets of BiVO<sub>4</sub> rapidly recombines with the holes in the VB of g-C<sub>3</sub>N<sub>4</sub> to form the interface Z-scheme heterostructure. That is, BiVO<sub>4</sub> surface heterojunction ultimately induces the formation of interface Z-scheme heterostructure. The interface Z-scheme heterostructure not only facilitates the space separation of the photo-generated carriers, but also accumulates electrons in the more negative potentiated CB of g-C<sub>3</sub>N<sub>4</sub> and holes in the more positive VB of \{110\} facets of BiVO<sub>4</sub>. Consequently, by means of the I-t, LSV and EIS measurements, the g-C<sub>3</sub>N<sub>4</sub>/\{010\} facets of BiVO<sub>4</sub> interface Z-scheme photocatalysts presents extraordinary photoelectrochemical performance. More importantly, the degradation rate of g-C<sub>3</sub>N<sub>4</sub>/\{010\} facets of BiVO<sub>4</sub> interface Z-scheme photocatalysts can reach the highest 88.3% within 30 min under visible light irradiation, and the mineralization ability (96.03%) is about 2.24 and 3.32 times as high as that of BiVO<sub>4</sub> (42.83%) and g-C<sub>3</sub>N<sub>4</sub> (28.89%), respectively.

### 1. Introduction

With increasing environmental pollution and energy crises, semiconductor-based heterogeneous photocatalysis has attracted worldwide attention due to its application in solar energy conversion and environmental remediation [1–3]. However, the rapid recombination and weak redox ability of photogenerated carriers result in low photocatalytic efficiency and limit its practical applications. Therefore, the key to improving the photocatalytic performance is to overcome the aforementioned problems [4].

Recent investigations on crystal facet engineering of semiconductors have proved that the exposed highly active crystalline facets of semiconductors can promote the photocatalytic activity. Li et al. demonstrated that effective charge separation could be achieved on different

crystal facets of BiVO<sub>4</sub>, and the photoinduced electrons and holes could migrate to \{010\} and \{110\} facets, respectively [5]. Yu et al. also reported that the \{110\} and \{001\} facets of anatase TiO<sub>2</sub> could form “surface heterojunctions” due to the different band structures and edge positions, which facilitated the effective separation of photogenerated carriers, and the enhanced photocatalytic activity [6]. However, for the single-component photocatalyst, the photo-excitation and separation process of the photo-induced electron-hole pairs on the same semiconductor, and carriers are apt to be bulk phase recombination. Compared with the single photocatalysts, the heterojunction photocatalysts usually display a higher photocatalytic activity because of the space separation of photogenerated electrons and holes [4].

The semiconductor heterostructures primarily include metal dopants, P-N heterojunctions and Z-scheme heterojunctions [7,8]. Among

\* Corresponding author.

E-mail address: tan3114@163.com (G. Tan).

them, Z-scheme heterostructures not only facilitate the effective spatial separation of photo-induced electron-hole pairs, but also enhance the redox ability of photocatalysts due to the increase in redox potential [4]. Therefore, the Z-scheme heterojunction photocatalyst has a good development potential.

The monoclinic BiVO<sub>4</sub> is a visible-light active photocatalyst with a narrow band gap of 2.40 eV. However, the photocatalytic ability of pure BiVO<sub>4</sub> is still not impressive because of the poor carrier transport properties and excessive recombination [9]. Graphitic carbon nitride (g-C<sub>3</sub>N<sub>4</sub>) has a good chemical stability and a large specific surface area due to its two-dimensional layered conjugate structure [10]. The g-C<sub>3</sub>N<sub>4</sub> with a band gap of 2.7 eV and the photogenerated electrons in the CB of g-C<sub>3</sub>N<sub>4</sub> possess strong reduction ability. Adversely, the holes with the low oxidant ability in the VB of g-C<sub>3</sub>N<sub>4</sub> are not enough to oxidize OH<sup>-</sup> to hydroxyl radicals reported by Wang et al [11]. Therefore, the photocatalytic performance of g-C<sub>3</sub>N<sub>4</sub> is limited.

In order to improve the photocatalytic performance of BiVO<sub>4</sub> semiconductor-based photocatalyst, BiVO<sub>4</sub> hybridized g-C<sub>3</sub>N<sub>4</sub> has attracted extensive attention due to the matching band edge position [12–14]. However, the Z-scheme heterostructure composed of the layered g-C<sub>3</sub>N<sub>4</sub> and {010} facets of BiVO<sub>4</sub> induced by BiVO<sub>4</sub> surface heterojunction have not yet been discussed. Herein, the monoclinic BiVO<sub>4</sub> with the co-exposed {010} and {110} facets were synthesized, which could form the surface heterojunction, and proposed that the layered g-C<sub>3</sub>N<sub>4</sub> and {010} facets of BiVO<sub>4</sub> formed a direct interface Z-scheme structure, resulting in the enhanced photocatalytic activity of the BiVO<sub>4</sub>.

## 2. Experimental

### 2.1. Preparation of the co-exposed {010} and {110} facets of BiVO<sub>4</sub>

First of all, 6 mmol Bi(NO<sub>3</sub>)<sub>3</sub>·5H<sub>2</sub>O was completely dissolved into 30 ml of 1 M HNO<sub>3</sub> aqueous solution, and stirred for 30 min at room temperature to form a solution. Second, 6 mmol NH<sub>4</sub>VO<sub>3</sub> was added into the solution with vigorous stirring for 2 h to get a precursor. Then it was added to Teflon-lined autoclaves with the packing ratio of 80%, maintaining at 70 °C for 15 h, and then naturally cooled until room temperature. The precipitates were filtered and washed with deionized water and ethanol, respectively for three times. Finally, the samples were dried at 80 °C for 12 h.

### 2.2. Preparation of g-C<sub>3</sub>N<sub>4</sub>/BiVO<sub>4</sub> hybrid photocatalysts

Pure g-C<sub>3</sub>N<sub>4</sub> was synthesized by calcining urea directly at 550 °C for 3 h in a semi-closed crucible with a lid in air atmosphere using a heating rate of 5 °C min<sup>-1</sup>. After being naturally cooled to room temperature, the pale-yellow g-C<sub>3</sub>N<sub>4</sub> was obtained.

The g-C<sub>3</sub>N<sub>4</sub>/BiVO<sub>4</sub> composites were obtained according to the following procedure: First, a certain amount of g-C<sub>3</sub>N<sub>4</sub> powder was added into deionized water to be magnetically stirred for 30 min at room temperature with the pH value is 5.03. Then, it was ultrasonically stirred for 1 h to completely disperse to form a suspension and the pH value is 5.01. After that, the BiVO<sub>4</sub> power was added into the g-C<sub>3</sub>N<sub>4</sub> suspension and stirred for 30 min under natural light. Then, the product was filtered and washed with deionized water and ethanol, respectively and dried at 70 °C to obtain g-C<sub>3</sub>N<sub>4</sub>/BiVO<sub>4</sub> coupled photocatalysts. The mass ratios of the resulting samples were as follows: g-C<sub>3</sub>N<sub>4</sub>: BiVO<sub>4</sub> = 2:8, 4:6 6:4, 8:2. The coupled photocatalysts with these different mass ratios were denoted here as B8G2, B6G4, B4G6, B2G8, respectively.

The crystalline structures of the samples were characterized by a powder X-ray diffraction (XRD; D/max-2200PC) with Cu K radiation in the range of 10–70°. The voltage and the applied current were 40 kV and 80 mA, respectively. The Raman scattering spectra (Renishaw invia) measurements were detected by excitations with 532 nm.

Infrared spectra were recorded on a Fourier transform infrared (FT-IR; VECTOR-22) spectrometer at room temperature by the standard KBr disk method. The surface analysis was performed by an X-ray photoelectron spectroscopy (XPS) (Model XSAM800, Shimadzu-Kratos Co., Ltd., Japan). The morphologies were observed on a field emission scanning electron microscopy (FE-SEM, S4800, Hitachi). The microstructures were examined by a transmission electron microscope and high-resolution transmission electron micrographs (TEM, TecnaiG2F20 S-TWIN, FEI). Thermogravimetric analysis of the samples was determined on a thermal analyzer in air with a heating rate of 5 °C/min from room temperature to 550 °C (TG, STA409PC, Germany). The zeta potential of the as-prepared samples was examined by a nano particle size and zeta potential analyzer (NANO-ZS, Malvern, U.K.). The UV-vis absorption spectra were obtained by a diffuse reflectance spectroscopy (DRS, Agilent Cary 5000) in the range of 200–800 nm, using BaSO<sub>4</sub> as the reference.

### 2.3. Computational details

All of the density functional calculations were investigated using the plane-wave pseudopotential method, implemented with the Cambridge Sequential Total Energy Package (CASTEP) code. The Perdew-Burke-Ernzerhof (PBE) of the generalized gradient approximation (GGA) was used to depict the exchange-correlation effects. The plane-wave cutoff energy was 400 eV for all the calculations. The k-point meshes were set as 6 × 6 × 3 of the bulk BiVO<sub>4</sub>, 3 × 6 × 1 of the {010} surface and 4 × 4 × 1 of the {110} surface. Interaction between the valence electrons and the ion core was substituted by an ultrasoft pseudopotential. The self-consistent convergence accuracy was set at 1 × 10<sup>-5</sup> eV per atom, the convergence criterion of the force between atoms was 0.03 eV/A, and the maximum displacement was 0.001 Å. The optimized lattice parameters of BiVO<sub>4</sub> were found to be a = 5.14 Å, b = 5.15 Å and c = 11.64 Å, in good agreement with experimental values (a = 5.19 Å, b = 5.09 Å and c = 11.70 Å). The {010} and {110} surface slabs were built with a bottom 5, 10 layers fixed and the top 5 and 10 layers relaxed, respectively. A vacuum layer of 12 Å was selected on each surface to eliminate the interactions between the surface atoms.

### 2.4. Evaluation of photocatalytic activity

The photocatalytic performance of all the prepared catalysts was evaluated by the degradation of Rhodamine B under visible light irradiation of a 500 W Xenon lamp, which was conducted in an XPA-7 photochemical reactor. The photocatalytic degradation products of RhB were examined by high performance liquid chromatography (HPLC, waters e2695) equipped with a UV-vis detector using a C18 inverted-phase column (250 × 4.6 mm, 5 m) at 550 nm. The mobile phase was a mixture of methanol and water (V:V = 6:4) with a flow rate of 0.8 mL min<sup>-1</sup>.

During the degradation experiment, a total of 0.05 g photocatalyst was added into 50 mL RhB solution (5 × 10<sup>-6</sup> mol/L) each time, and then the solution was stirred in darkness for 30 min before the illumination to achieve an adsorption-desorption equilibrium between the photocatalyst and RhB molecules. For a certain period of time, 5 mL of suspension was withdrawn regularly and centrifuged to remove the photocatalyst. Then the concentration of RhB supernatants was analyzed by a UV-vis spectrophotometer (SP-756p). Different contents of benzoquinone (BQ) (1 mmol), ethylene diamine tetraacetic acid-disodium salt (EDTA-2Na) (1 mmol), and tert-butyl alcohol (TBA) (0.3 mL) were introduced into the solution of RhB prior to catching ·O<sub>2</sub><sup>-</sup>, h<sup>+</sup>, and ·OH, respectively.

### 2.5. Photoelectrochemical analysis

All the photoelectrochemical measurements were executed on an electrochemical work station (CHI660E), using a standard three-

electrode cell with the as-prepared samples as the working electrode, a platinum wire as the counter electrode, and the saturated Ag/AgCl electrode as a reference electrode. The preparation method of electrodes would be presented in detail as follows: 0.1 g of samples was added into the mixed solution of 1 mL of anhydrous ethanol and 0.1 mL of acetyl acetone, and a uniform suspension was obtained with the ultrasonic dispersion. Then, the as-prepared suspension was spread on a  $1.5 \times 2 \text{ cm}^2$  fluorine-doped tin oxide (FTO) conducting glass with spin-coating method for twice. The film electrodes were dried under ambient condition and then calcinated at  $70^\circ\text{C}$  for 3 h. A 500 W Xe arc lamp was used as the visible light source. A 0.1 M  $\text{Na}_2\text{SO}_4$  aqueous solution was used as the electrolyte. Photocurrent curves were recorded by an amperometric method under intermittent irradiation. The linear scan voltammetry (LSV) and the cyclic voltammetry (CV) were recorded at a scan rate of 50 mV/s. Electrochemical impedance spectra (EIS) were obtained in the frequency range of 0.01–100,000 Hz and then interpreted by a nonlinear least-squares fitting procedure using a commercial software (ZsimpWin). A 500 W Xe lamp was used as the light source for visible light irradiation in photoelectrochemical analyses.

### 2.6. Analyses of hydroxyl radicals

The formation of hydroxyl radicals ( $\cdot\text{OH}$ ) on the surface of the photo-illuminated sample was detected using photoluminescence (PL) method with terephthalic acid (TA) as a probe molecule [15]. Terephthalic acid, a poor fluorescent molecule, readily reacted with  $\cdot\text{OH}$  to produce a highly fluorescent product named 2-hydroxyterephthalic acid (TA-OH). The method depended on the PL signal in the visible light region at 435 nm arising from TA-OH. The PL intensity of TA-OH was positive related to the amount of  $\cdot\text{OH}$  produced in the solution. The experimental process was as follows: at room temperature, 0.1 g of the photocatalyst powder was distributed in a blend aqueous solution of  $5 \times 10^{-4}$  M TA and  $2 \times 10^{-3}$  M NaOH. The formation of hydroxyl radicals ( $\cdot\text{OH}$ ) on the surface of illuminated samples was detected by photoluminescence (PL) method. The irradiation was continuous and the sampling was carried out every 5 min for analyses. The PL spectra of the generated TA-OH were obtained using an Edinburgh FS5 fluorescence spectrophotometer.

## 3. Results and discussions

### 3.1. Characterizations of $\text{g-C}_3\text{N}_4/\text{BiVO}_4$ composites

**Fig. 1a** is the reflective pattern of  $\text{g-C}_3\text{N}_4$  prepared through calcining urea. The strongest diffraction peak (002) at around  $27.4^\circ$  is a characteristic inter-planar stacking peak of conjugated aromatic systems, corresponding to a distance  $d = 0.336 \text{ nm}$ , where the stacking is

extraordinarily tighter than the packing in carbon with graphene units ( $d = 0.353 \text{ nm}$ ) [16]. The higher packing density perpendicular to the layers for aromatic systems with heteroatom substitution is well comprehended and can be ascribed to the localization of the electrons and the stronger binding between the layers. Another pronounced additional peak is found at  $13.1^\circ$  with an interlayer spacing of  $0.672 \text{ nm}$  presumably correlated to an in-planar structural packing motif, such as the hole-to-hole distance of the nitride pores in the crystal [17]. Moreover, the weak diffraction peaks of intermediates (e.g. cyanuric acid, melem and melom) appear in the XRD patterns, which may be due to incomplete pyrolysis [18,19].

In addition, the shape and the position of the  $\text{BiVO}_4$  characteristic peaks in the composite have little change (**Fig. 1b**), which is similar to the XRD patterns of the pure  $\text{BiVO}_4$ , that is to say, the introduction of the layered  $\text{g-C}_3\text{N}_4$  has no effects on  $\text{BiVO}_4$  crystalline structures. No other new peaks are examined in all the samples, revealing that no impurities are formed in the preparation process. The XRD results indicate that  $\text{g-C}_3\text{N}_4$  and  $\text{BiVO}_4$  co-exist in the composite photocatalysts.

Raman spectra analysis of as-prepared samples is performed to demonstrate the interaction between the  $\text{BiVO}_4$  and  $\text{g-C}_3\text{N}_4$ , as shown in **Fig. 2**. The vibrational bands of pristine  $\text{BiVO}_4$  at approximate  $213 \text{ cm}^{-1}$ ,  $328 \text{ cm}^{-1}$  and  $830 \text{ cm}^{-1}$  are observed, which are in agreement with the previous report [20]. The  $\text{g-C}_3\text{N}_4$  displays a broad Raman spectrum in the range of  $1300$ – $2200 \text{ cm}^{-1}$ , attributed to the breathing modes of the s-triazine ring in the CN network [21]. As for all composite photocatalysts, the intensity of characteristic band related to the pristine  $\text{BiVO}_4$  at  $830 \text{ cm}^{-1}$  assigned to the asymmetric and symmetric V–O stretching modes is slightly decreased, and red shifts are observed (**Fig. 2b**). Furthermore, the characteristic peak intensity of  $\text{g-C}_3\text{N}_4$  is not increased with further increase in the amount of  $\text{g-C}_3\text{N}_4$  (**Fig. 2a**). Nevertheless, for the mechanically mixed B2G8, the peak of the  $\text{BiVO}_4$  is significantly decreased, but the shift does not occur, and the intensity of the  $\text{g-C}_3\text{N}_4$  peaks is significantly increased. The above results illustrate that there exist strong interactions between the  $\text{BiVO}_4$  and  $\text{g-C}_3\text{N}_4$  by ultrasonic dispersion method.

The FT-IR spectra of  $\text{BiVO}_4$ ,  $\text{g-C}_3\text{N}_4$  and  $\text{g-C}_3\text{N}_4/\text{BiVO}_4$  hybrid are shown in **Fig. 3**. For pure monoclinic  $\text{BiVO}_4$ , the vibrational band at  $739 \text{ cm}^{-1}$  can be assigned to asymmetric stretching vibration of the  $\nu_3$  ( $\text{VO}_4$ ) [22]. The absorption band of the pure  $\text{g-C}_3\text{N}_4$  at  $1639 \text{ cm}^{-1}$  can be ascribed to the C–N stretching vibration modes. The four strong vibrational bands at  $1573$ ,  $1543$ ,  $1461$  and  $1410 \text{ cm}^{-1}$  are indicative of the typical stretching mode of CN heterocycle. The bands at  $1317$  and  $1238 \text{ cm}^{-1}$  are related to the stretching vibration of connected units of C–N(–C)–C (full condensation) or C–NH–C (partial condensation) [23], respectively. The band at  $812 \text{ cm}^{-1}$  is originated out of the plane skeletal bending modes of the triazine cycles. The broad absorption band within  $3000$ – $3300 \text{ cm}^{-1}$  is assigned to the N–H stretching

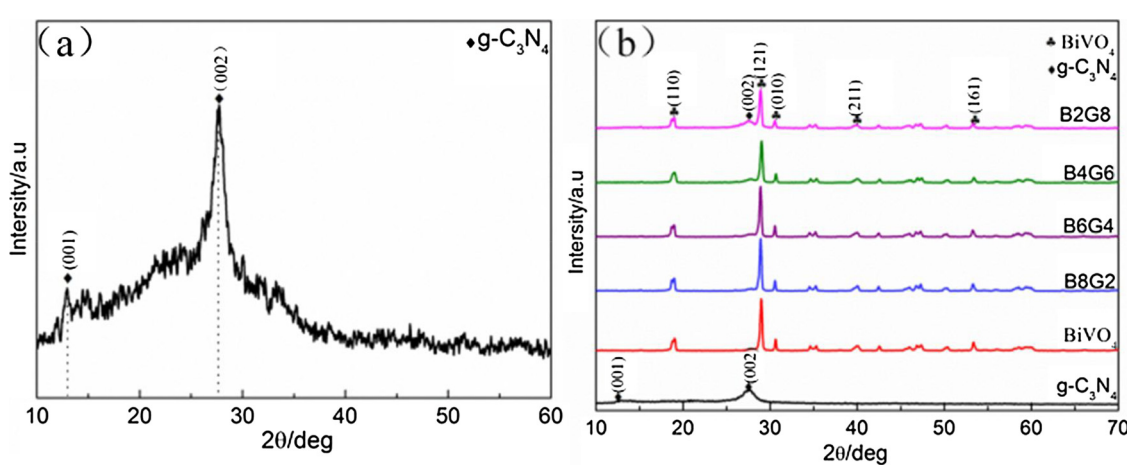


**Fig. 1.** (a) XRD patterns of  $\text{g-C}_3\text{N}_4$  (b) XRD patterns of  $\text{g-C}_3\text{N}_4/\text{BiVO}_4$  photocatalysts.

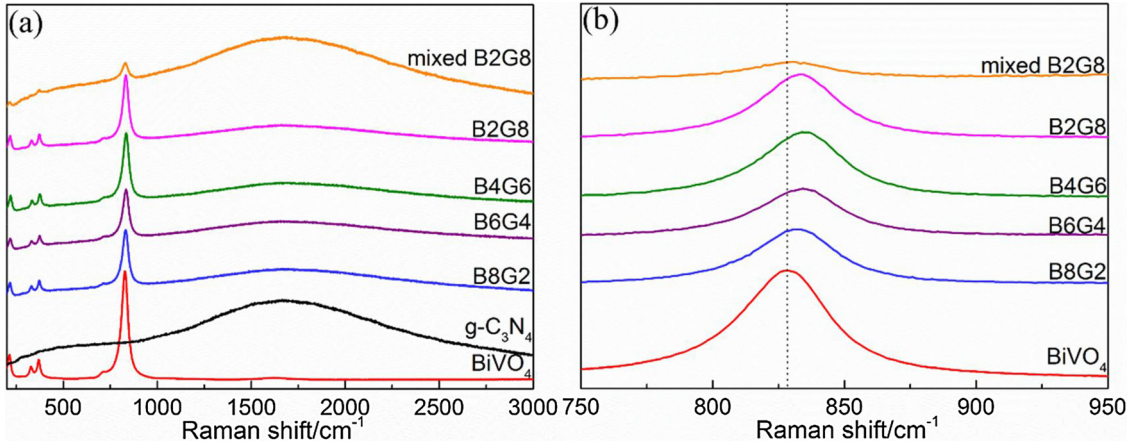


Fig. 2. (a) Raman spectra of g-C<sub>3</sub>N<sub>4</sub>/BiVO<sub>4</sub> photocatalysts with different mass ratios, (b) the magnified Raman peaks of g-C<sub>3</sub>N<sub>4</sub>/BiVO<sub>4</sub> photocatalysts.

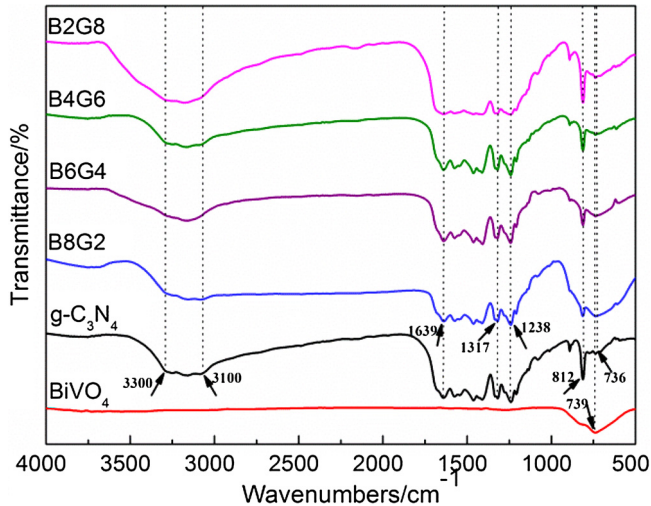


Fig. 3. FT-IR spectra of g-C<sub>3</sub>N<sub>4</sub>/BiVO<sub>4</sub> photocatalysts with different mass ratios.

vibration of the residual NH (or NH<sub>2</sub>) group which is the residual amino (C—NH<sub>2</sub> or 2C—NH) with incomplete polymerization after the calcining process or O—H stretching associated with adsorbed water [24]. It is obvious that the primary bands of g-C<sub>3</sub>N<sub>4</sub> and BiVO<sub>4</sub> are included in hybrid photocatalysts, implying that the g-C<sub>3</sub>N<sub>4</sub>/BiVO<sub>4</sub> heterojunction is fabricated successfully. Additionally, the relative intensity of g-C<sub>3</sub>N<sub>4</sub> at 812 cm<sup>-1</sup> in the composite photocatalysts is increased with the content of g-C<sub>3</sub>N<sub>4</sub>, and the characteristic band of BiVO<sub>4</sub> is slightly blue shifted from 739 cm<sup>-1</sup> to 736 cm<sup>-1</sup>, implying the interfacial interaction between the g-C<sub>3</sub>N<sub>4</sub> and BiVO<sub>4</sub> [25,26].

To further confirm the interaction between g-C<sub>3</sub>N<sub>4</sub> and BiVO<sub>4</sub>, XPS analysis is performed to detect the chemical states of BiVO<sub>4</sub>, g-C<sub>3</sub>N<sub>4</sub> and B2G8 photocatalysts (Fig. 4). The full surface survey XPS spectrum is presented in Fig. 4a, which confirms the presence of various elements (Bi, V, O, C, and N) on the surface of the samples. In the Bi 4f spectra (Fig. 4b), the peaks of BiVO<sub>4</sub> at 159.1 eV and 164.4 eV are assigned to Bi 4f<sub>7/2</sub> and Bi 4f<sub>5/2</sub> of Bi<sup>3+</sup> induced by Bi<sup>3+</sup> species, respectively [27]. However, those peaks in the spectrum of B2G8 are shifted to 158.8 eV and 164.1 eV, respectively. For O 1 s spectra (Fig. 4c), the peaks at 532.4 eV corresponding to the V—O of the BiVO<sub>4</sub>, are shifted to 532.7 eV in the B2G8 composite photocatalysts. The XPS spectra of C 1s are observed in Fig. 4d, and the binding energy centered at 284.6 eV is assigned to the adventitious hydrocarbon from the XPS instrument itself, whereas the other C 1s peak occurring at 288.3 eV is indicative of the sp<sup>2</sup>-hybridized carbon in N-containing aromatic ring (N—C=N) [28]. The peaks of C 1s for B2G8 are shifted toward lower binding

energies relative to pure g-C<sub>3</sub>N<sub>4</sub>. The shifts in XPS measurement could be attributed to the chemical environment change arising from the strong interaction between BiVO<sub>4</sub> and g-C<sub>3</sub>N<sub>4</sub> [29], which is in good agreement with the Raman and FT-IR results.

To investigate the morphology and the structure information of the as-prepared samples, SEM and TEM images are examined as depicted Fig. 5. It can be observed that the morphology of the pure BiVO<sub>4</sub> crystals exhibits the decagonal shape and mainly exposes two facets, which is denoted as {010} and {110} facets, respectively (Fig. 5a, b). In addition, the DFT electronic structure calculations of {010} and {110} facets are shown in Fig. 6a. The Fermi level of {010} facets is still located at the top of the valence band of {010} surface. However, the Fermi level of {110} facets enter their valence band. The differences of the energy levels in the conduction bands ( $\Delta$  CB) and the valence bands ( $\Delta$  VB) between the {010} and {110} facets are calculated at ca. 0.37 and 0.31 V (vs. NHE, pH = 7), respectively. Although the calculated difference may be much larger than the actual value, the existing difference well demonstrates the energy level discrepancy between {010} and {110} facets. Because the {010} and {110} facets of BiVO<sub>4</sub> contact each other, their Fermi levels should be equal. So, the {010} and {110} facets can form surface heterojunction (Fig. 6b), which will induce the electrons and holes transfer to {010} and {110} facets, respectively [5,6]. The wrinkled layered structure of the pure g-C<sub>3</sub>N<sub>4</sub> possibly includes several stacking layers, suggesting the planar graphitic-like structure (Fig. 5c), and the TEM image of g-C<sub>3</sub>N<sub>4</sub> is more obvious (Fig. 5d), which is consistent with the XRD results. It is clear that the layered g-C<sub>3</sub>N<sub>4</sub> is anchored on the {010} facets of BiVO<sub>4</sub> selectively (Fig. 5e, f). The TEM image (Fig. 5g) clearly shows the contact interface between BiVO<sub>4</sub> and g-C<sub>3</sub>N<sub>4</sub>. The lattice fringes of 0.467 nm correspond to the {110} facets of the monoclinic BiVO<sub>4</sub> (Fig. 5h), which further proves that the layered g-C<sub>3</sub>N<sub>4</sub> is anchored to the {010} facets rather than {110} facets. The contact interface between the g-C<sub>3</sub>N<sub>4</sub> and {010} facets of BiVO<sub>4</sub> serves as the center of the photoinduced electron-hole pairs recombination, which reduces the distance of electron transfer [5]. Therefore, the g-C<sub>3</sub>N<sub>4</sub>/BiVO<sub>4</sub> hybrid photocatalysts is expected to reveal the enhanced photocatalytic performance.

In order to investigate the phase transformation during pyrolysis of urea, TG-DSC analyses are carried out to investigate the phase transformation during pyrolysis of urea. As shown in Fig. 7, the strongest endothermic peak at 134 °C is the melting point of urea. The peak at 185 °C, and the weight loss of 48.45 wt% between 140 °C and 210 °C, which is originated at a stage of urea destruction, and the formation of cyanuric acid [30]. The endothermic peak appears at 240 °C, and the weight loss of 36 wt% from 210 to 250 °C would be due to the sublimation and decomposition of some small molecules derived from urea pyrolysis, such as melamine [31]. The peak at 346 °C and the weight loss of 38.1 wt% from 270 to 420 °C implies that the thermal

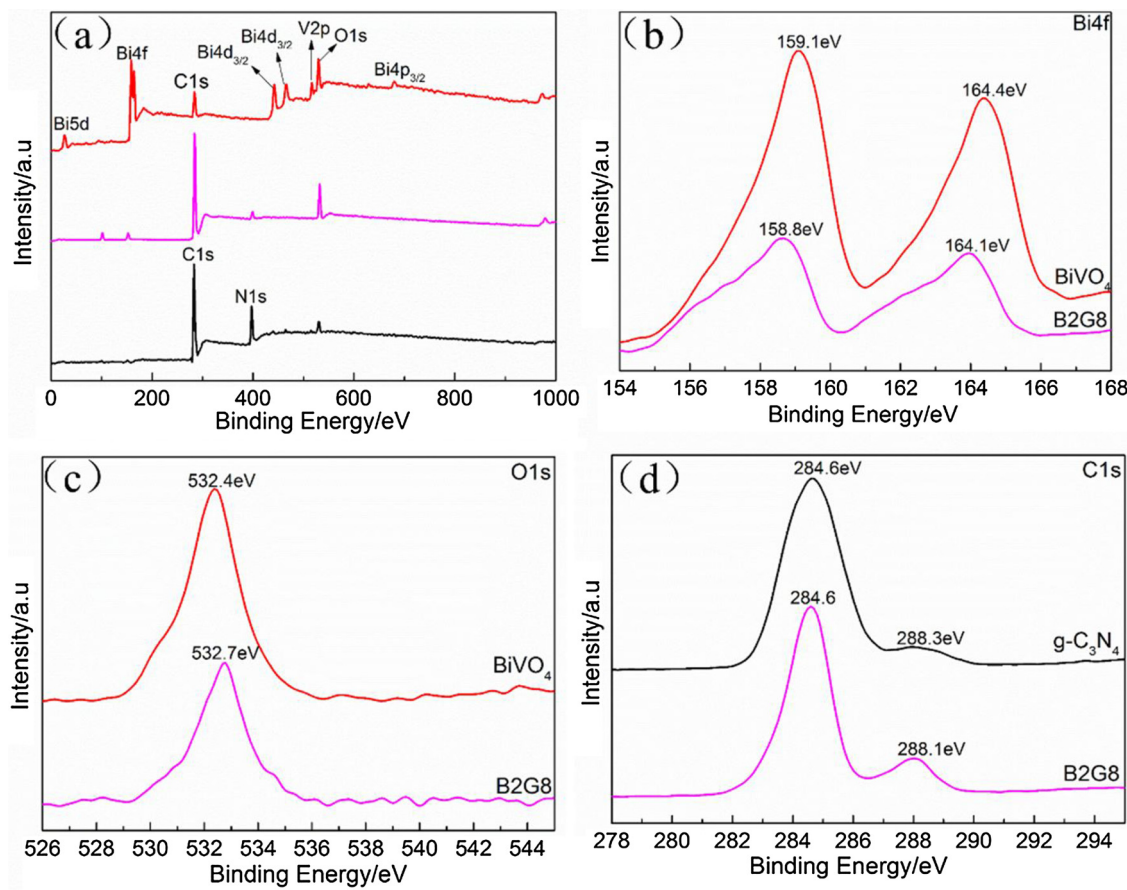
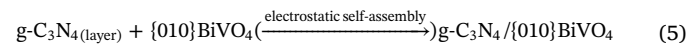
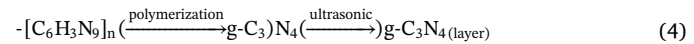
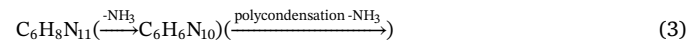
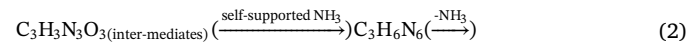
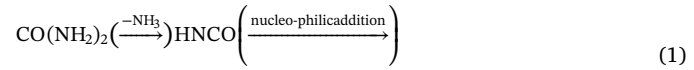


Fig. 4. (a) XPS survey spectra of  $\text{BiVO}_4$ ,  $\text{g-C}_3\text{N}_4$  and B2G8, (b) Bi 4f, (c) O 1s and (d) C 1s.

polymerization condensation of melamine into melam occurs in this temperature range. The further slight weight loss from 450 to 550 °C can be ascribed to the phase formation from melam to  $\text{g-C}_3\text{N}_4$  [32].

The deduction about the growth process is shown in Fig. 8. Urea ( $\text{CO}(\text{NH}_2)_2$ ) is first pyrolysed to isocyanic acid (HNCO) at low temperature (< 200 °C) (Eq. (1)) [31]. Subsequently, isocyanic acid is converted into cyanuric acid, which further turns into melamine by self-supported  $\text{NH}_3$  (Eq. (2)) [33]. Melamine can be condensed to form melam via self-condensation, which undergoes polymerization and is rearranged at about 390 °C to form melem ( $\text{C}_6\text{H}_6\text{N}_{10}$ ) (Eq. (3)) [34]. When the temperature reaches approximately 500 °C, melem is further pyrolyzed and condensed to form melon ( $-\text{[C}_6\text{H}_3\text{N}_9\text{]_n}$ ) with low polymerization degrees [31]. These polymers at 520–550 °C are further condensed to form higher polymerization degrees graphite-like carbon nitride ( $\text{g-C}_3\text{N}_4$ ) (Eq. (4)) [16]. The  $\text{g-C}_3\text{N}_4$  possesses a graphite-like structure, with weak van der Waals force and hydrogen bonds between C–N layers, which can be overcome by stirring and ultrasonic treatment with the polar water molecules as a solvent. Therefore, the stacked multilayered  $\text{g-C}_3\text{N}_4$  is exfoliated into the layered  $\text{g-C}_3\text{N}_4$ . Moreover, the surface energy of  $\text{g-C}_3\text{N}_4$  is reduced because the agreement with the surface energy of  $\text{H}_2\text{O}$  leads to the very stable solution of ultrathin layered  $\text{g-C}_3\text{N}_4$  [35]. The layered  $\text{g-C}_3\text{N}_4$  with a positive zeta potential (+13.4 mV) at pH 5.03, the result is similar to what Zhu et al. reported [36]. The co-exposed {010} and {110} facets of  $\text{BiVO}_4$  is slowly added to the  $\text{g-C}_3\text{N}_4$  suspension with stirring and ultrasonic treatment under natural light. As a consequence, electrons tend to transfer to {010} facets which lead to {010} facets with negative charge, and holes migrate to {110} facets to make it with positive charge. Thus, the layered  $\text{g-C}_3\text{N}_4$  is anchored on the {010} facets of  $\text{BiVO}_4$  to form a heterogeneous structure by such an electrostatic self-assembly approach (Eq. (5)).



### 3.2. Photocatalytic activity analyses

Fig. 9a illustrates that the UV-vis absorption spectra are changed during the photocatalytic degradation of RhB under visible irradiation by co-exposed {010} and {110} facets of  $\text{BiVO}_4$ . The maximum absorption peak is slightly decreased at 554 nm with the increase of illumination time. In addition, there is no obvious shift on the maximum absorption band of RhB. The absorption peak of B2G8 samples sharply decreases and the tiny blue shift occurs (Fig. 9b). The photocatalytic performance of  $\text{g-C}_3\text{N}_4/\{010\}$  facets  $\text{BiVO}_4$  photocatalysts with different mass ratios is investigated as shown in Fig. 9c. The degradation rate of RhB is only 22.66% of the co-exposed {010} and {110} facets of  $\text{BiVO}_4$ . As expected, the  $\text{g-C}_3\text{N}_4/\{010\}$  facets  $\text{BiVO}_4$  hybrid photocatalysts exhibits significantly the enhanced photocatalytic activity. Particularly, when the content of  $\text{g-C}_3\text{N}_4$  is 80 wt%, the B2G8 sample demonstrates the highest photocatalytic activity of 88.3% in 30 min under visible light irradiation, exceeding that of pure  $\text{BiVO}_4$  (22.66%) by a factor of 4, and the apparent rate constant is  $0.0673 \text{ min}^{-1}$  (Fig. 9c, d). In contrast to the hybrid photocatalysts, the photocatalytic

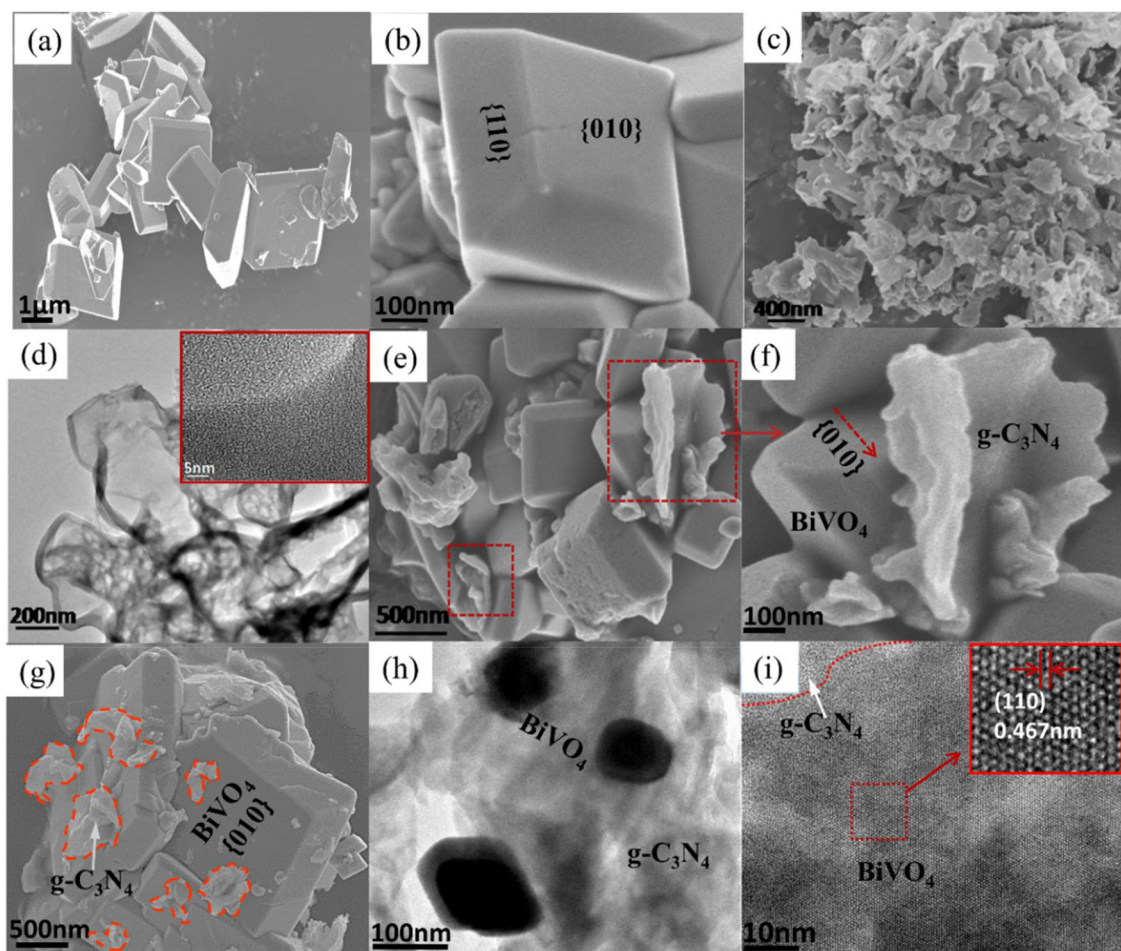


Fig. 5. SEM, TEM and HRTEM images of (a, b)  $\text{BiVO}_4$ , (c, d)  $\text{g-C}_3\text{N}_4$ , (e, f, g, h, i) B2G8.

activity of the mechanically mixed B2G8 is slightly higher than that of  $\text{BiVO}_4$ , but much lower than that of B2G8. The above results clearly demonstrate that the strong interfacial interaction between the layered  $\text{g-C}_3\text{N}_4$  and  $\{010\}$  facets of  $\text{BiVO}_4$  greatly improves the photocatalytic performance.

The photochemical stability of photocatalysts is investigated by performing recycling experiments under repeated visible light irradiation. Fig. 10a shows that after four consecutive runs, no apparent

deactivation of the B2G8 hybrid photocatalysts is observed, illustrating its excellent stability under visible light irradiation. The XRD patterns before and after repeated irradiation are compared (Fig. 10b). It can be seen that the phase is unchanged, that is to say, the photocatalysts crystal structures is not damaged. The SEM image of B2G8 hybrid photocatalysts after repeated visible light irradiation shows that the  $\text{g-C}_3\text{N}_4$  is still selectively anchored on the  $\{010\}$  facets of  $\text{BiVO}_4$  (the inset of Fig. 10b), which suggests that electrostatic attraction stability is

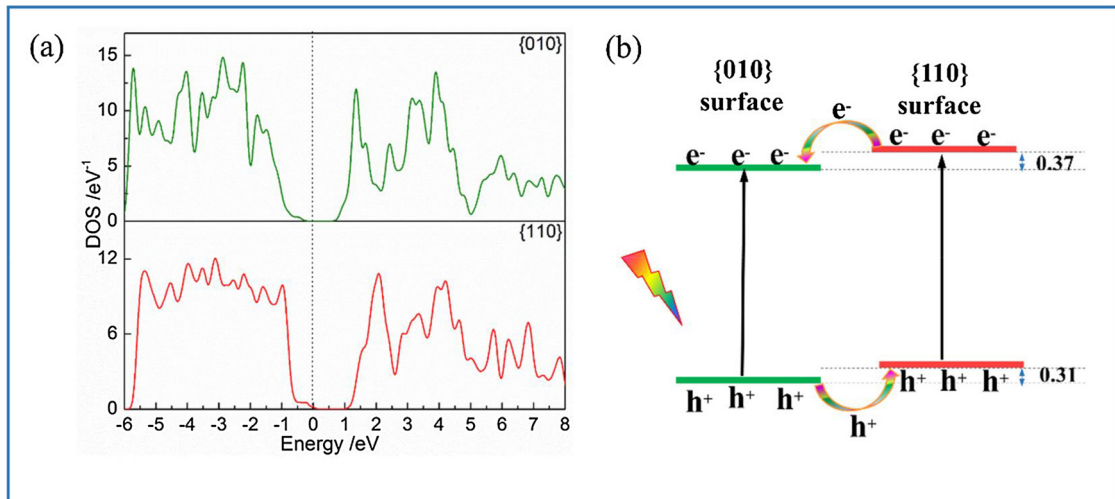


Fig. 6. (a) Density of states (DOS) plots for  $\{010\}$  and  $\{110\}$  facets of  $\text{BiVO}_4$ , (b) the surface heterojunction formed by  $\{010\}$  and  $\{110\}$  facets of  $\text{BiVO}_4$ .

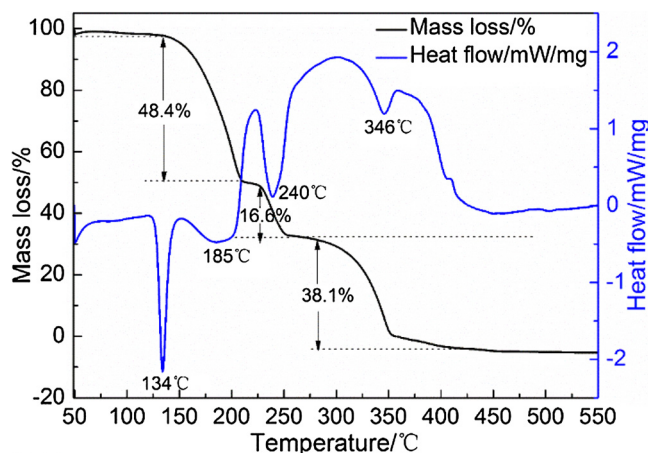


Fig. 7. TG-DSC thermograms for heating urea.

excellent.

### 3.3. Photoelectrochemical analyses

The transient photocurrent indirectly reflects the separation efficiency of photogenerated carriers during the photoreactions [37]. In Fig. 11a, the transient photocurrent response of BiVO<sub>4</sub>, B8G2 and B2G8 photocatalysts with several on-off cycles of intermittent illumination is compared. It can be seen that the photocurrent of all the samples reaches a constant value when the light is on. Contrarily, the photocurrent is rapidly decreased to zero as soon as the light is turned off, which reveals a good reproducibility of all the samples. As for pristine BiVO<sub>4</sub>, the photocurrent curve has an anodic spike at the initial time of illumination. After reaching the peak, the continuous decrease in the

photocurrent proceeds until a constant photocurrent is achieved. This photocurrent decay is related to the recombination processes of electron-hole pairs [38]. During the decay, the holes accumulated at the BiVO<sub>4</sub> surface are competitively recombined with electrons from conduction band, instead of being trapped or captured by reduced species in the electrolyte. The photocurrent becomes constant after the equilibration of competitive separation and recombination of electron-hole pairs. However, the anodic photocurrent spike is not observed from the hybrid photocatalysts, especially, the stable photocurrent value of the B2G8 sample is about 1.2 times as high as that of pure BiVO<sub>4</sub>. Linear sweep voltammogram (LSV) measurement is performed to measure the photocurrent response of this composite catalyst in comparison with pure BiVO<sub>4</sub> under visible light irradiation (Fig. 11b). The photocurrent of BiVO<sub>4</sub> is too small to be identified in comparison with other hybrid photocatalysts. Significantly, g-C<sub>3</sub>N<sub>4</sub>/ {010} facets BiVO<sub>4</sub> electrodes exhibits larger photocurrent response than bare BiVO<sub>4</sub>. B2G8 hybrid photocatalysts achieve the highest photocurrent response. The above results suggest that the contact interface between g-C<sub>3</sub>N<sub>4</sub> and {010} facets of BiVO<sub>4</sub> can promotes the faster interfacial charge transfer as well as an effective separation of photogenerated carriers, which should be the major reason to enhance their photocatalytic activities.

In addition, the electrochemical impedance (EIS) is also an effective method for the analyses of the enhanced charge separation efficiency. Fig. 12 plots that the impedance arc radii of BiVO<sub>4</sub>, B8G2 and B2G8 samples in the dark are obviously larger than those under visible light illumination, suggesting that there are fewer electrons across the electrolyte interface in the dark condition [39]. To gain more precise information, the specified fit values of circuit components are listed in Table 1. The equivalent circuit model (the inset of Fig. 12a) includes the solution resistance (RL), the space charge capacitance (C), the electrochemical double-layer capacitance (Q) and the charge transfer resistance (R) which are the main research objects. The R values of BiVO<sub>4</sub>,

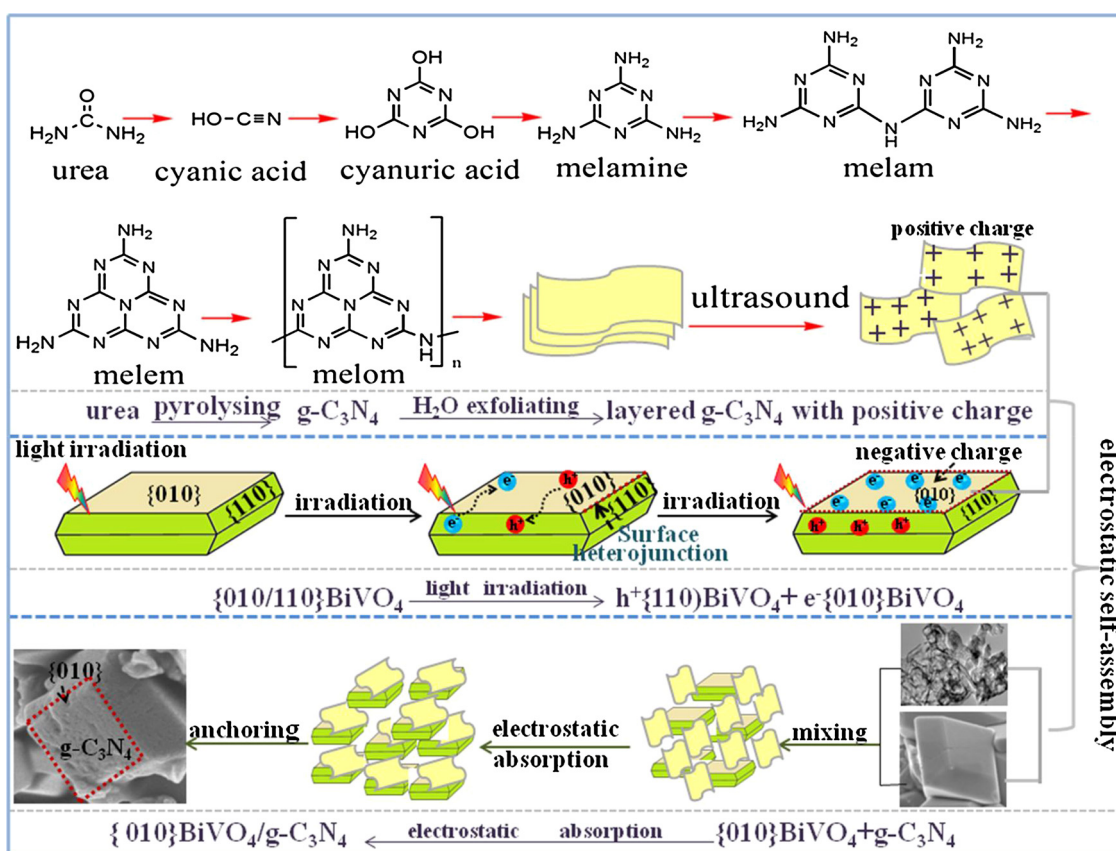
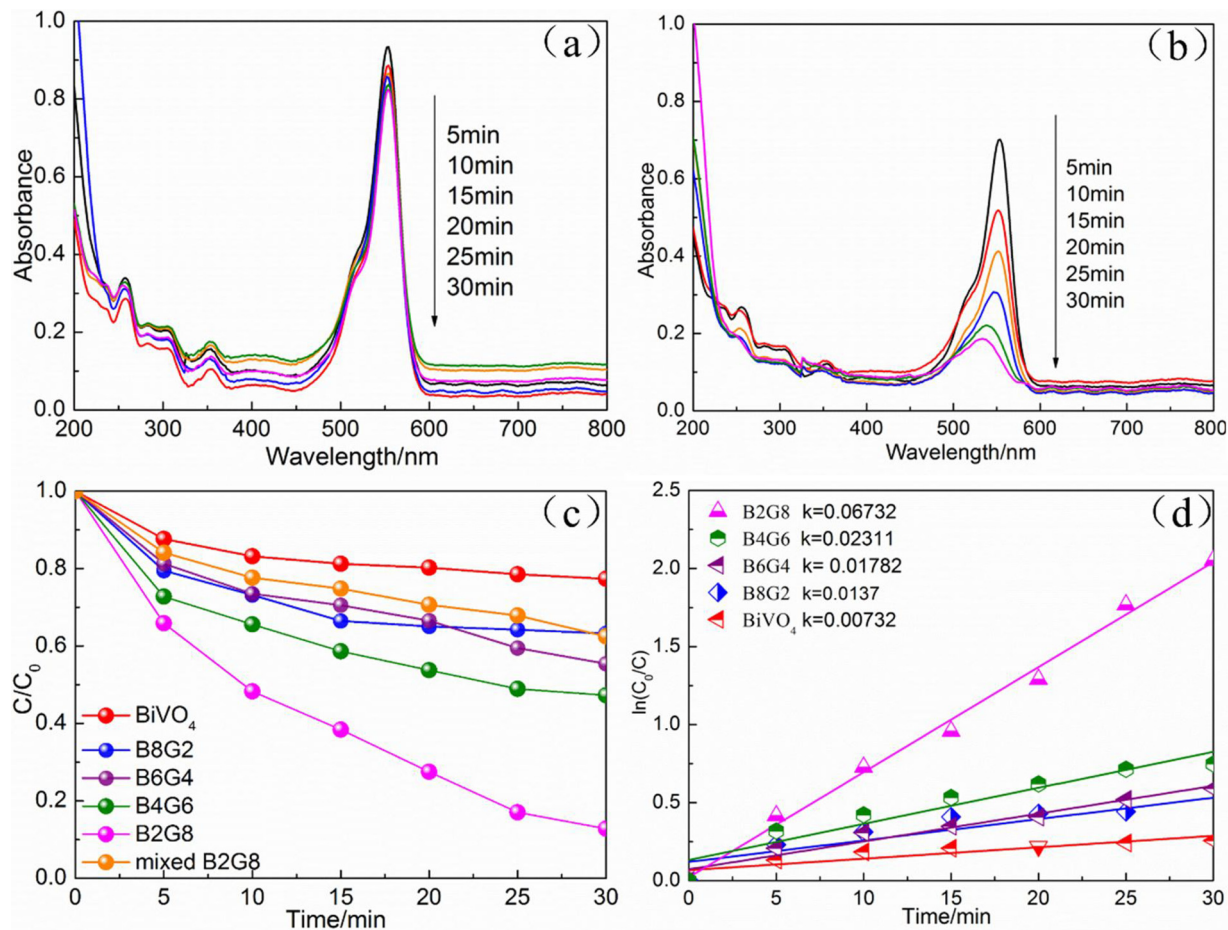


Fig. 8. The possible growth mechanism over g-C<sub>3</sub>N<sub>4</sub>/ {010} facets BiVO<sub>4</sub> photocatalysts.



**Fig. 9.** UV-vis absorption spectral changes of the photocatalytic degradation of RhB by (a) pure BiVO<sub>4</sub> and (b) B2G8, (c) the photodegradation of all the catalysts under visible-light irradiation, (d) the dynamics of RhB photodegradation reaction ( $\ln(C_0/C)$ ).

B8G2 and B2G8 samples are reduced from  $2.93 \times 10^5 \Omega$ ,  $2.52 \times 10^5 \Omega$  and  $2.59 \times 10^5 \Omega$  to  $2.73 \times 10^5 \Omega$ ,  $1.97 \times 10^5 \Omega$  and  $1.04 \times 10^5 \Omega$  under visible light irradiation, respectively. The results prove the fastest transfer and the separation efficiency of photogenerated charge in the B2G8 coupled photocatalysts, which is consistent with the photocatalytic activities.

#### 3.4. Photocatalytic mechanism analyses

In order to get insights into the photocatalytic mechanism, the active species trapping experiments are carried out to examine the effective active species during the photodegradation process [40]. It is clear that the photocatalytic performance is reduced by 26.54%, 51.76% and 80% with TBA, BQ, and EDTA-2Na, respectively (Fig. 13). Thus, it could be concluded that  $\cdot\text{OH}$  and  $\cdot\text{O}_2^-$  are the main reactive

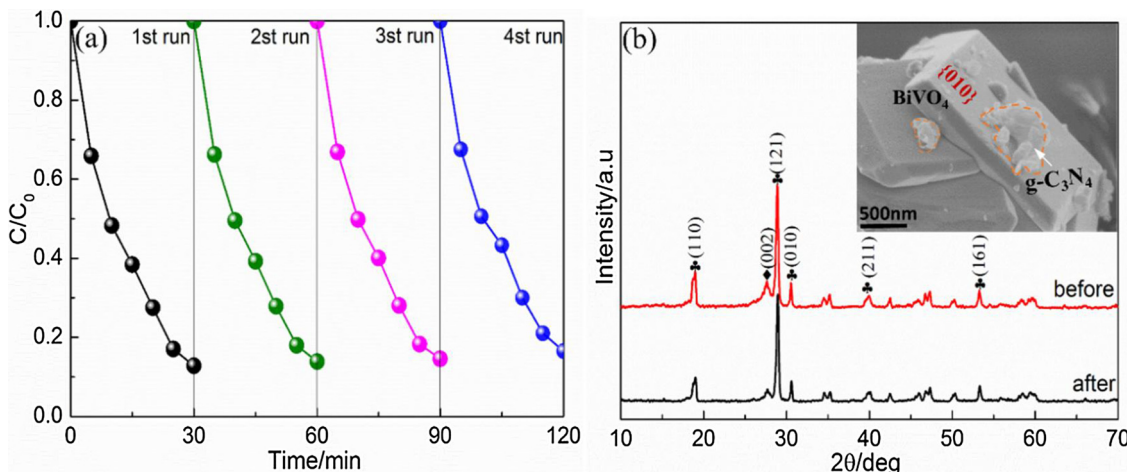


**Fig. 10.** (a) Cycling runs of B2G8 for the degradation of RhB under visible light irradiation, (b) XRD patterns of B2G8 before and after 4th run cycle photocatalytic experiments, (the inset is the SEM image after 4th repeated irradiation).

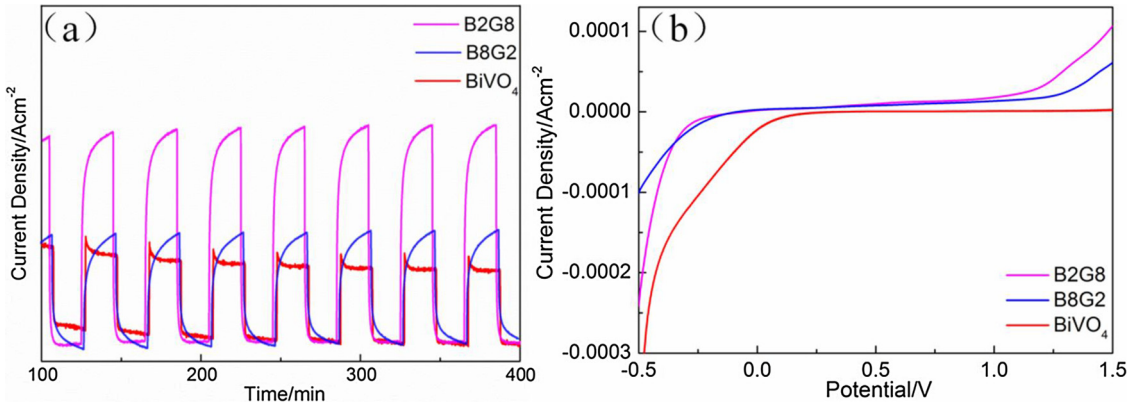


Fig. 11. (a) The transient photocurrent responses of as-prepared samples; (b) The current-voltage curves as-prepared samples.

species, while  $h^+$  contributes a little during the degradation process.

Diffuse reflectance is used to investigate the energy band structure to further understand the photocatalytic mechanism. As shown in Fig. 14a, all the samples exhibit the steep shape, which manifests that the visible-light absorption is not due to the transition from the impurity level, but due to the band-gap transition [41]. The valence bands of the monoclinic BiVO<sub>4</sub> is resulting from the hybrid orbital of Bi 6s and O 2p, and the conduction band is composed of 3d empty orbital of V<sup>5+</sup> in VO<sub>4</sub><sup>3-</sup> tetrahedron composition [42]. The absorption edge of the synthesized monoclinic BiVO<sub>4</sub> is about at 556 nm. The intrinsic absorption band of g-C<sub>3</sub>N<sub>4</sub> originates from the electron transition from the valence band (VB) derived from N2p orbitals to the conduction band (CB) formed by C2p orbitals [43], and the absorption edge at around 444 nm. The absorption edge of g-C<sub>3</sub>N<sub>4</sub>/ {010} facets BiVO<sub>4</sub> photocatalysts with a slight red shift is compared with that of the pure BiVO<sub>4</sub>, which can be attributed to the introduction of the N 2p state around the Fermi level [44]. Furthermore, the composite photocatalysts exhibits similar absorption features as pristine BiVO<sub>4</sub>, implying that g-C<sub>3</sub>N<sub>4</sub> hybrid with BiVO<sub>4</sub> at the interface is not incorporated into the lattice of BiVO<sub>4</sub>, which is consistent with the XRD and SEM results. The band gaps are elevated by the following formula [45]:

$$\alpha h\nu = A(h\nu - E_g)^{n/2}$$

where  $\alpha$ ,  $h\nu$ , and  $A$  are absorption coefficient, Planck constant, light frequency, and a constant, respectively. In addition, according to Lambert-Beer Law:  $A = cbc$ , where  $b$  and  $c$  are optical path ( $\sim 1 \text{ cm}^{-1}$ ), sample concentration, respectively. The  $n$  values of BiVO<sub>4</sub> (direct-gap semiconductor) and g-C<sub>3</sub>N<sub>4</sub> (indirect-gap semiconductor) are 1 and 4 [46,47]. Taking  $\alpha h\nu^{1/2}$  and  $\alpha h\nu^2$  as the function of  $h\nu$  as displayed in Fig. 14b. Through data fitting, the  $E_g$  values of BiVO<sub>4</sub> (2.41 eV) and g-C<sub>3</sub>N<sub>4</sub> (2.69 eV) can be obtained.

Furthermore, the valence and the conduction band edge potential can be determined by the following equations [48]:

$$\text{ECB} = \lambda - E_e - 0.5E_g$$

$$\text{EVB} = E_e + \text{ECB}$$

where  $\lambda$  is the electronegativity of the semiconductor, EVB is the VB potential, ECB is the CB potential, and  $E_e$  is about 4.5 V (vs. NHE, pH = 7). The position of the valence and the conduction band of BiVO<sub>4</sub> are 2.865 and 0.455 V (vs. NHE, pH = 7), respectively. In addition, a slight difference in the position of the valence and the conduction band between {010} and {110} facets of BiVO<sub>4</sub> (Fig. 6). The valence and the conduction band of g-C<sub>3</sub>N<sub>4</sub> are 1.515 and -1.175 V (vs. NHE, pH = 7), respectively. According to the band edge positions, the valence band offset (VBO) and the conduction band offset (CBO) between g-C<sub>3</sub>N<sub>4</sub> and BiVO<sub>4</sub> are approximately 1.515 and -1.175 V (vs. NHE, pH = 7), suggesting that the g-C<sub>3</sub>N<sub>4</sub>/ {010} facets BiVO<sub>4</sub> is a staggered band alignment structure. The {010} facets of BiVO<sub>4</sub> with negative charge and the layered g-C<sub>3</sub>N<sub>4</sub> with positive charge lead to forming a built-in electric field at interface. The work function (WF) of BiVO<sub>4</sub> is higher than that of the WF of g-C<sub>3</sub>N<sub>4</sub>, so the electric field direction is from g-C<sub>3</sub>N<sub>4</sub> to {010} facets of BiVO<sub>4</sub> [49,50], which facilitates to migrate the photoexcited electrons from the CB of {010} facets of BiVO<sub>4</sub> to VB of g-C<sub>3</sub>N<sub>4</sub>, which results in the recombination of electrons. Simultaneously, the built-in electric field also suppresses the photoinduced electrons in the CB of g-C<sub>3</sub>N<sub>4</sub> to flow into the CB of {010} facets of BiVO<sub>4</sub>. As a result, the photogenerated electrons in the CB of {010} facets of BiVO<sub>4</sub> and the holes in the VB of g-C<sub>3</sub>N<sub>4</sub> are recombined, which facilitates the photoexcited electrons and holes pairs naturally aggregated in the CB of g-C<sub>3</sub>N<sub>4</sub> and VB of {010} facets of BiVO<sub>4</sub> to occur redox reaction. The above analyses illustrate that g-C<sub>3</sub>N<sub>4</sub>/ {010} facets BiVO<sub>4</sub> photocatalysts is a direct interface Z-scheme heterostructure.

On the basis of the above band analysis, a possible photocatalytic mechanism of the improved photocatalytic activity of the g-C<sub>3</sub>N<sub>4</sub>/ {010} facets BiVO<sub>4</sub> interface Z-scheme photocatalysts is tentatively proposed and schematically illustrated in Fig. 15. Due to the different band

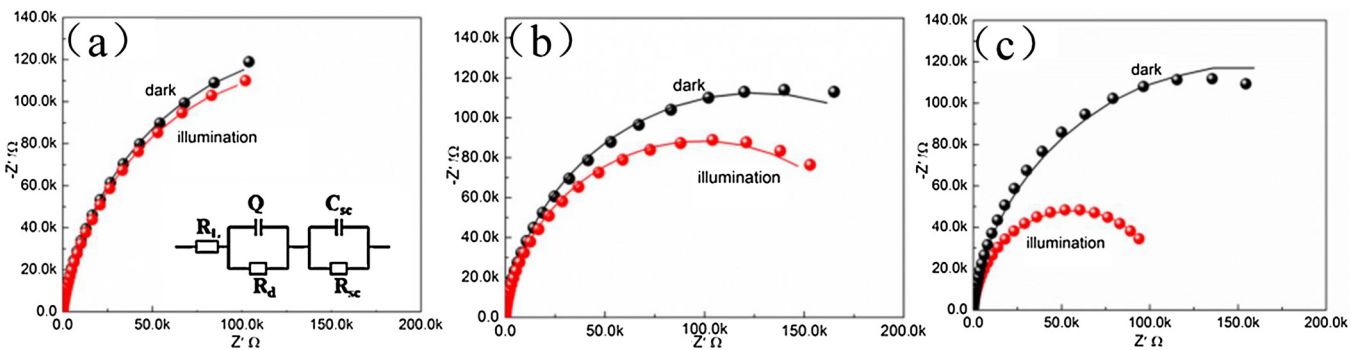
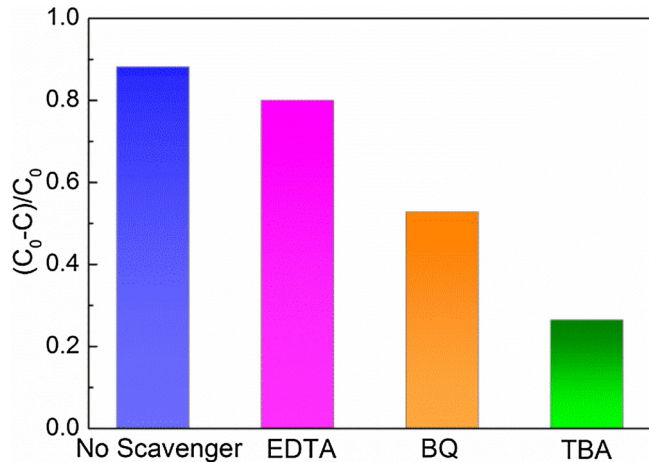


Fig. 12. EIS Nyquist plots (dot) and Z-fit equivalent circuit (curves) of (a) BiVO<sub>4</sub>, (b) B8G2 (c) B2G8 samples. The solid line traces correspond to the fitting using the equivalent circuit in the inset of Fig. 7a.

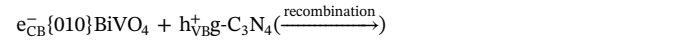
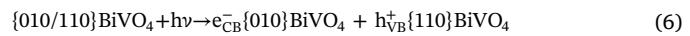
**Table 1**Z-Fit Equivalent Circuit Data of BiVO<sub>4</sub>, B8G2 and B2G8 films.

CDC code	R <sub>L</sub> (Ω)	R(×10 <sup>5</sup> Ω)	error	C(×10 <sup>-5</sup> F)	Q(×10 <sup>-5</sup> Ssec <sup>n</sup> )	n
BiVO <sub>4</sub> (Dark)	30.44	2.93	1.69%	1.358	4.518	0.862
BiVO <sub>4</sub> (Vis)	31.08	2.73	1.83%	1.421	4.633	0.857
B8G2 (Dark)	32.45	2.52	1.33%	1.523	2.261	0.888
B8G2 (Vis)	32.50	1.97	1.17%	1.481	2.221	0.893
B2G8 (Dark)	29.61	2.59	1.87%	1.979	1.915	0.841
B2G8 (Vis)	22.08	1.04	2.63%	2.817	1.468	0.758

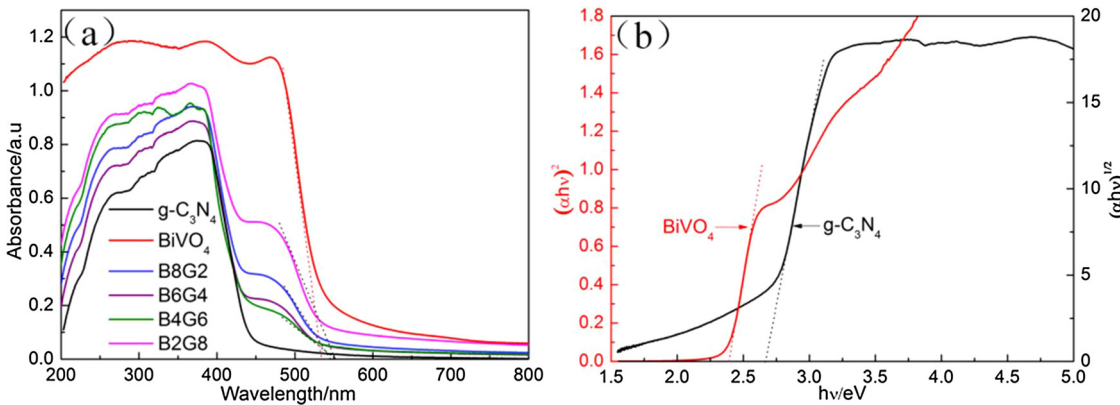
**Fig. 13.** Photocatalytic degradation of RhB over B2G8 photocatalysts with the addition of BQ, TBA, and EDTA.

structures and the edge positions, the co-exposed {010} and {110} facets of BiVO<sub>4</sub> can form surface heterojunction, which promotes the {010} facets of BiVO<sub>4</sub> with negative charge (Eq. (6)), whereas g-C<sub>3</sub>N<sub>4</sub> with positive charge. Thus, layered g-C<sub>3</sub>N<sub>4</sub> is anchored on the {010} facets of BiVO<sub>4</sub> through strong interface electrostatic interaction, which leads to form a built-in electric field at the contact interface. Under the built-in electric field driving, photogenerated electrons in the CB of {010} facets of BiVO<sub>4</sub> rapidly recombine with the holes in the VB of g-C<sub>3</sub>N<sub>4</sub> to form the interface Z-scheme heterostructure (Eq. (7)). The interface Z-scheme heterostructure not only facilitates the space separation of the photogenerated carriers, but also accumulates electrons in the CB of g-C<sub>3</sub>N<sub>4</sub> and holes in the VB of {110} facets of BiVO<sub>4</sub> respectively. Consequently, the more positive holes in the VB of {110} facets of BiVO<sub>4</sub> produce the rich active ·OH radicals with powerful oxidation (Eq. (8)), the more negative potentiated electrons in the CB of g-C<sub>3</sub>N<sub>4</sub> reduce the molecular oxygen to yield ·O<sub>2</sub><sup>−</sup> (Eq. (9)), and then induce the RhB degradation (Eqs. (10) and (11)). Therefore, the

photocatalytic performance of g-C<sub>3</sub>N<sub>4</sub>/ {010} facets BiVO<sub>4</sub> interface Z-scheme heterostructure can be significantly enhanced.



To further prove that g-C<sub>3</sub>N<sub>4</sub>/ {010} facets BiVO<sub>4</sub> hybrid photocatalysts form the direct interface Z-scheme heterostructure, hydroxyl radicals (·OH) are detected by the PL method using terephthalic acid (TA) as a probe molecule. As clearly seen from Fig. 16, the barely PL signal appears on the irradiation of the pure g-C<sub>3</sub>N<sub>4</sub> samples, suggesting that OH<sup>−</sup> is not generated because the valence band position of g-C<sub>3</sub>N<sub>4</sub> (1.515 V (vs. NHE, pH = 7)) is insufficient to oxidize OH<sup>−</sup> to hydroxyl radicals (E(OH<sup>−</sup>/·OH) = 2.4 V (vs. NHE, pH = 7) [12]). A significant increase in PL intensity at approximate 435 nm of B2G8 samples is investigated with the increase of illumination time and is much higher than that of the pure BiVO<sub>4</sub>. If the co-exposed {010} and {110} facets of BiVO<sub>4</sub> and g-C<sub>3</sub>N<sub>4</sub> form the traditional heterostructure, the photo-induced electrons are probably transferred from the CB of g-C<sub>3</sub>N<sub>4</sub> to the CB of {010} facets of BiVO<sub>4</sub>, and the holes are likely migrated from the VB of {110} facets of BiVO<sub>4</sub> to the VB of g-C<sub>3</sub>N<sub>4</sub>. This heterojunction can lead to efficient space separation of carriers. However, the holes in the VB of g-C<sub>3</sub>N<sub>4</sub> are inadequate to oxidize the surface OH<sup>−</sup> or adsorb water molecules to form ·OH. Therefore, the traditional g-C<sub>3</sub>N<sub>4</sub>/ {010} facets BiVO<sub>4</sub> heterostructure exhibits the lower fluorescence intensity than that of the pure BiVO<sub>4</sub>, which is disagreement with the hydroxyl radical experiments. It is assumed that g-C<sub>3</sub>N<sub>4</sub> and {010} facets of BiVO<sub>4</sub> do not form a traditional heterojunction, but undoubtedly to form the mediator-free direct interface Z-scheme heterojunction.

**Fig. 14.** (a) UV-vis diffuse reflectance spectra of g-C<sub>3</sub>N<sub>4</sub>/BiVO<sub>4</sub> coupled photocatalysts with different mass ratios, (b) plots of the  $(\alpha h\nu)^{1/2}$  vs photon energy ( $h\nu$ ) for g-C<sub>3</sub>N<sub>4</sub>, (c)plots of the  $(\alpha h\nu)^2$  vs photon energy ( $h\nu$ ) for BiVO<sub>4</sub>.

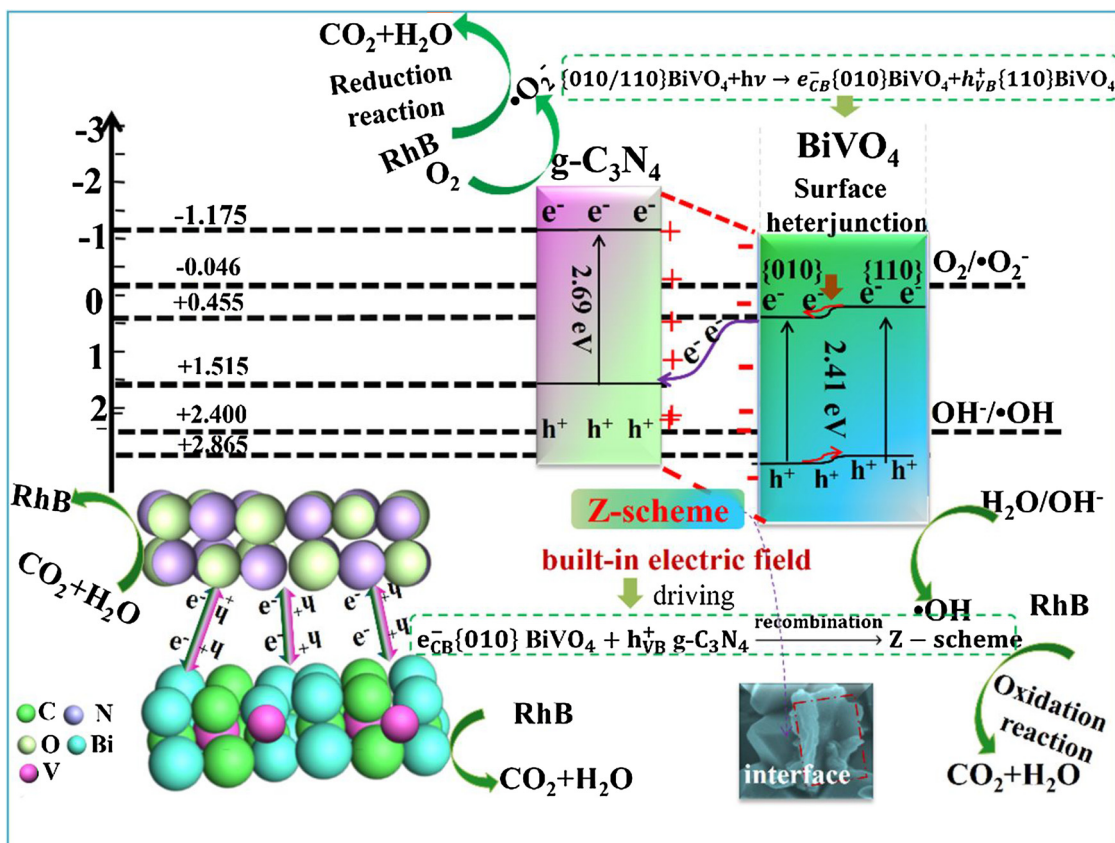


Fig. 15. The possible photocatalytic enhanced mechanism over  $\text{g-C}_3\text{N}_4/\{010\}$  facets  $\text{BiVO}_4$  interface Z-scheme photocatalysts under visible light irradiation.

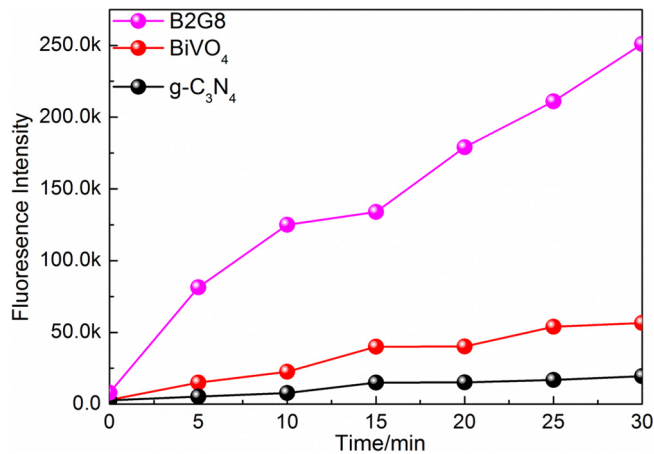


Fig. 16. Comparison of PL intensity at 435 nm against irradiation time of  $\text{BiVO}_4$ ,  $\text{g-C}_3\text{N}_4$ , and B2G8 samples.

The enhancement of redox ability of hybrid photocatalysts can be further verified by photocatalytic mineralization. Fig. 17a–c displays the mineralization of RhB in the presence of  $\text{BiVO}_4$ ,  $\text{g-C}_3\text{N}_4$  and B2G8 during 30 min visible light irradiation. Five main components  $N,N$ -diethyl- $N$ -ethyl-rhodamine (DER),  $N$ -ethyl- $N'$ -ethylrhodamine (EER),  $N,N$ -diethyl-rhodamine (DR),  $N$ -ethyl-rhodamine (ER), rhodamine (R) are detected [51]. As irradiation time is increased, the intensity of DER peak is decreased, indicating the degradation of RhB into small molecules. However, the amount of other degradation products, such as DER, EER, DR, ER and R which are formed from the further de-ethylation of DER are almost stable during the degradation process. These results indicate that DER is the main intermediate during the degradation of RhB [52]. The mineralization rate is only 42.83% and

28.89% of  $\text{BiVO}_4$  and  $\text{g-C}_3\text{N}_4$ , respectively (Fig. 17a, b). However, the mineralization ability of the B2G8 can reach 96.03% (Fig. 17c), which is about 2.24 and 3.32 times as high as that of  $\text{BiVO}_4$  (42.83%) and  $\text{g-C}_3\text{N}_4$  (28.89%), respectively. The efficient mineralization of B2G8 hybrid photocatalysts is due to the formation of interface Z-scheme heterostructure with strong redox ability.

Furthermore, the reduction ability of the as prepared  $\text{g-C}_3\text{N}_4/\{010\}$  facets  $\text{BiVO}_4$  photocatalysts are well evident from the cyclic voltammograms [53]. As shown in Fig. 17d, no obvious reduction peak can be observed on the bare  $\text{BiVO}_4$ , likely because the CB potential of  $\text{BiVO}_4$  is lower than the standard potential of  $\text{O}_2/\cdot\text{O}_2^-$  ( $-0.046$  V vs. NHE, pH = 7)) [54]. It's worth noting that the pure  $\text{g-C}_3\text{N}_4$  and  $\text{g-C}_3\text{N}_4/\{010\}$  facets  $\text{BiVO}_4$  composite photocatalysts exhibit specific reduction peak, which seems to be the reduction of adsorbed oxygen. Significantly, B2G8 photocatalysts shows the strongest reduction peak with a slight shift, indicating the strongest reduction ability [55]. This result further demonstrates that  $\text{g-C}_3\text{N}_4$  and  $\{010\}$  facets of  $\text{BiVO}_4$  forms the interface Z-scheme photocatalysts.

#### 4. Conclusion

The  $\text{g-C}_3\text{N}_4/\{010\}$  facets  $\text{BiVO}_4$  interface Z-scheme photocatalysts is fabricated by ultrasonic dispersion method. The co-exposed  $\{010\}$  and  $\{110\}$  facets of  $\text{BiVO}_4$  can form surface heterojunction, which promotes the  $\{010\}$  facets of  $\text{BiVO}_4$  with negative charge, whereas layered  $\text{g-C}_3\text{N}_4$  with positive charge. Thus, layered  $\text{g-C}_3\text{N}_4$  is anchored on the  $\{010\}$  facets of  $\text{BiVO}_4$  through strong interface electrostatic interaction, which leads to form a built-in electric field at the contact interface. That is to say,  $\text{BiVO}_4$  surface heterojunction ultimately induces the formation the interface Z-scheme heterostructure without an electron mediator. The direct interface Z-scheme heterostructure not only facilitates the space separation of the photogenerated carriers, but also accumulates

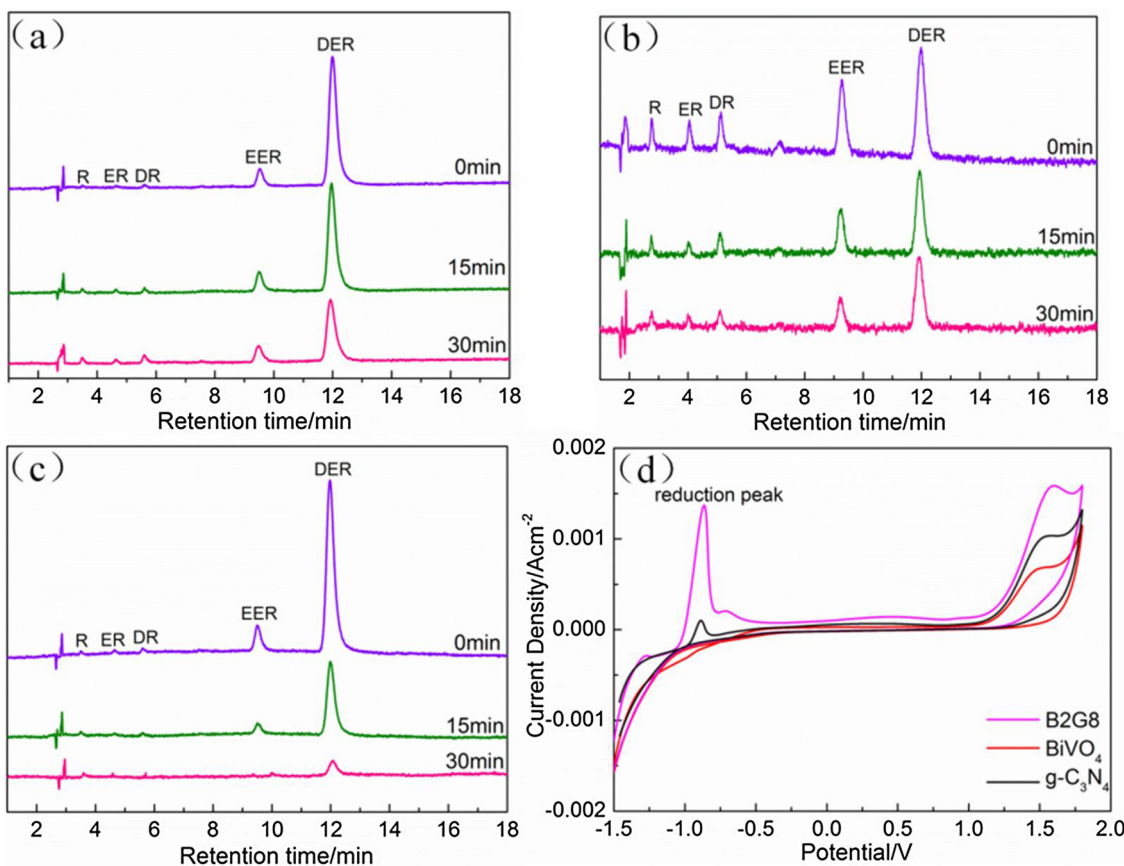


**Fig. 17.** HPLC chromatograms of RhB photodegradation under visible light irradiation: (a) BiVO<sub>4</sub>, (b) g-C<sub>3</sub>N<sub>4</sub>, (c) B2G8; (d) The current-voltage curves of BiVO<sub>4</sub>, g-C<sub>3</sub>N<sub>4</sub>, and B2G8 samples under visible light.

electrons in the CB of g-C<sub>3</sub>N<sub>4</sub> and holes in the VB of {110} facets of BiVO<sub>4</sub> respectively. The more negative potentiated electrons in the CB of g-C<sub>3</sub>N<sub>4</sub> reduce the molecular oxygen to yield ·O<sub>2</sub><sup>−</sup>. Under the induction of the surface heterojunction formed by the co-exposed {010} and {110} facets of BiVO<sub>4</sub>, the photogenerated holes are accumulated in the VB of {110} facets with more negative potential to oxidize OH<sup>−</sup> or in the surface adsorbed water to produce rich active ·OH radicals. In composite system, the ·O<sub>2</sub><sup>−</sup> with the strong reduction ability and ·OH with the strong oxidizing ability to induce the RhB degradation together. Therefore, the degradation rate of g-C<sub>3</sub>N<sub>4</sub>/ {010} facets BiVO<sub>4</sub> interface Z-scheme photocatalysts can reach the highest 88.3% within 30 min under visible light irradiation, and the mineralization ability (96.03%) is about 2.24 and 3.32 times as high as that of BiVO<sub>4</sub> (42.83%) and g-C<sub>3</sub>N<sub>4</sub> (28.89%), respectively.

## Acknowledgements

This work is supported by the Project of the National Natural Science Foundation of China (Grant No. 51772180), the Academic Leaders Funding Scheme of Shaanxi University of Science & Technology (2013XSD06) and the Graduate Innovation Fund of Shaanxi University of Science and Technology (SUST-A04).

## References

- [1] Q.F. Zhang, E. Uchaker, S.L. Candelaria, G.Z. Cao, Chem. Soc. Rev. 42 (2013) 3127–3171.
- [2] M. Xu, L. Han, S. Dong, ACS Appl. Mater. Interfaces 5 (2013) 12533–12540.
- [3] S.B. Wang, X.C. Wang, Appl. Catal. B-Environ. 162 (2015) 494–500.
- [4] P. Zhou, J. Yu, M. Jaroniec, Adv. Mater. 26 (2014) 4920–4935.
- [5] R. Li, F. Zhang, D. Wang, J. Yang, M. Li, J. Zhu, X. Zhou, H. Han, C. Li, Nat. Commun. 4 (2013) 1432.
- [6] J.G. Yu, J.X. Low, W. Xiao, P. Zhou, M. Jaroniec, J. Am. Chem. Soc. 136 (2014) 8839–8842.
- [7] G. Yang, D.M. Chen, H. Ding, J.J. Feng, J.Z. Zhang, Y.F. Zhu, S. Hamid, D.W. Bahnemann, Appl. Catal. B-Environ. 219 (2017) 611–618.
- [8] R. Marschall, Adv. Funct. Mater. 24 (2014) 2421–2440.
- [9] W.Z. Wang, X.W. Huang, S. Wu, Y.X. Zhou, L.J. Wang, H.L. Shi, Y.J. Liang, B. Zou, Appl. Catal. B-Environ. 134 (2013) 293–301.
- [10] Y.Y. Wang, W.J. Yang, X.J. Chen, J. Wang, Y.F. Zhu, Appl. Catal. B-Environ. 220 (2018) 337–347.
- [11] F.Z. Su, S.C. Mathew, G. Lipner, X.Z. Fu, M. Antonietti, S. Blechert, X.C. Wang, J. Am. Chem. Soc. 132 (2010) 16299–16301.
- [12] M. Ou, Q. Zhong, S.L. Zhang, L.M. Yu, J. Alloy Compd. 626 (2015) 401–409.
- [13] Y.X. Ji, J.F. Cao, L.Q. Jiang, Y.H. Zhang, Z.G. Yi, J. Alloy Compd. 590 (2014) 9–14.
- [14] J. Zhao, J.H. Yan, H.J. Jia, S.W. Zhang, X.Y. Zhang, L. Xu, J. Mol. Catal. A-Chem. 424 (2016) 162–170.
- [15] J.G. Yu, Q. Li, S.W. Liu, M. Jaroniec, Chem. Eur. J. 19 (2013) 2433–2441.
- [16] A. Thomas, A. Fischer, F. Goettmann, M. Antonietti, J.O. Müller, R. Schlögl, J.M. Carlsson, J. Mater. Chem. A 18 (2008) 4893–4908.
- [17] F. Goettmann, A. Fischer, M. Antonietti, A. Thomas, Angew. Chem. Int. Ed. 45 (2006) 4467–4471.
- [18] B. Jurgens, E. Irran, J. Senker, P. Kroll, H. Muller, W. Schnick, J. Am. Chem. Soc. 125 (2003) 10288–10300.
- [19] C. Zhao, G. Tan, J. Huang, W. Yang, H. Ren, A. Xia, ACS Appl. Mater. Interfaces 7 (2015) 23949–23957.
- [20] J. Yu, A. Kudo, Adv. Funct. Mater. 16 (2006) 2163–2169.
- [21] Y. Fu, J. Zhu, C. Hu, X. Wu, X. Wang, Nanoscale 6 (2014) 12555–12564.
- [22] R.L. Frost, D.A. Henry, M.L. Weier, W. Martens, J. Raman Spectrosc. 37 (2006) 722–732.
- [23] S. Zhou, Y. Liu, J. Li, Y. Wang, G. Jiang, Z. Zhao, D. Wang, A. Duan, J. Liu, Y. Wei, Appl. Catal. B-Environ. 158 (2014) 20–29.
- [24] Y.C. Zhao, Z. Liu, W.G. Chu, L. Song, Z.X. Zhang, D.L. Yu, Y.J. Tian, S.S. Xie, L.F. Sun, Adv. Mater. 20 (2008) 1777–1781.
- [25] Z. Huang, Q. Sun, K. Lv, Z. Zhang, M. Li, B. Li, Appl. Catal. B-Environ. 164 (2015) 420–427.
- [26] G. Tan, L. She, T. Liu, C. Xu, H. Ren, A. Xia, Appl. Catal. B-Environ. 207 (2017) 120–133.
- [27] P. Madhusudan, J. Ran, J. Zhang, J. Yu, G. Liu, Appl. Catal. B-Environ. 110 (2011) 286–295.
- [28] X. Bai, L. Wang, R. Zong, Y. Zhu, J. Phys. Chem. C 117 (2013) 9952–9961.
- [29] X. Song, Y. Hu, M. Zheng, C. Wei, Appl. Catal. B-Environ. 182 (2016) 587–597.
- [30] A. Kharlamov, M. Bondarenko, G. Kharlamova, N. Gubareni, Diam. Relat. Mater. 66 (2016) 16–22.

- [31] P.M. Schaber, J. Colson, S. Higgins, D. Thielen, B. Anspach, J. Brauer, *Thermochim. Acta* 424 (2004) 131–142.
- [32] F. Dong, M. Ou, Y. Jiang, S. Guo, Z. Wu, *Ind. Eng. Chem. Res.* 53 (2014) 2318–2330.
- [33] A.M. Bernhard, D. Peitz, M. Elsener, A. Wokaun, O. Kroecher, *Appl. Catal. B-Environ.* 115 (2012) 129–137.
- [34] J. Xu, H. Wu, X. Wang, B. Xue, Y. Li, Y. Cao, *Phys. Chem. Chem. Phys.* 15 (2013) 4510–4517.
- [35] X. Zhang, X. Xie, H. Wang, J. Zhang, B. Pan, Y. Xie, *J. Am. Chem. Soc.* 135 (2013) 18–21.
- [36] B. Zhu, P. Xia, W. Ho, J. Yu, *Appl. Surf. Sci.* 344 (2015) 188–195.
- [37] K. Lv, X. Li, K. Deng, J. Sun, X. Li, M. Li, *Appl. Catal. B-Environ.* 95 (2010) 383–392.
- [38] J.G. Yu, T.T. Ma, S.W. Liu, *Phys. Chem. Chem. Phys.* 13 (2011) 3491–3501.
- [39] F.X. Xiao, S.F. Hung, H.B. Tao, J. Miao, H.B. Yang, B. Liu, *Nanoscale* 6 (2014) 14950–14961.
- [40] Y.Y. Zhu, Y.J. Wang, Q. Ling, Y.F. Zhu, *Appl. Catal. B-Environ.* 200 (2017) 222–229.
- [41] A. Kudo, I. Tsuji, H. Kato, *Chem. Commun.* 17 (2002) 1958–1959.
- [42] C. Karunakaran, S. Kalaiavani, P. Vinayagamoorthy, S. Dash, *Mater. Sci. Semicond. Process.* 21 (2014) 122–131.
- [43] L. Ye, D. Wang, S. Chen, *ACS Appl. Mater. Interfaces* 8 (2016) 5280–5289.
- [44] J.H. Zhang, F.Z. Ren, M.S. Deng, Y.X. Wang, *Phys. Chem. Chem. Phys.* 17 (2015) 10218–10226.
- [45] M.A. Butler, *J. Appl. Phys.* 48 (1977) 1914–1920.
- [46] L. Zhou, W. Wang, S. Liu, L. Zhang, H. Xu, W. Zhu, *J. Mol. Catal. A-Chem.* 252 (2006) 120–124.
- [47] Y. Wang, Y. Di, M. Antonietti, H. Li, X. Chen, X. Wang, *Chem. Mater.* 22 (2010) 5119–5121.
- [48] M.L. Guan, D.K. Ma, S.W. Hu, Y.J. Chen, S.M. Huang, *Inorg. Chem.* 50 (2011) 800–805.
- [49] J.H. Zhang, F.Z. Ren, M.S. Deng, Y.X. Wang, *Phys. Chem. Chem. Phys.* 17 (2015) 10218–10226.
- [50] J. Liu, B. Cheng, J. Yu, *Phys. Chem. Chem. Phys.* 18 (2016) 31175–31183.
- [51] P. Tao, Y. Xu, C. Song, Y. Yin, Z. Yang, S. Wen, S. Wang, H. Liu, S. Li, C. Li, T. Wang, M. Shao, *Sep. Purif. Technol.* 179 (2017) 175–183.
- [52] C. Mu, Y. Zhang, W. Cui, Y. Liang, Y. Zhu, *Appl. Catal. B-Environ.* 212 (2017) 41–49.
- [53] N. Iqbal, I. Khan, Z.H.A. Yamani, A. Qurashi, *Sol. Energy* 144 (2017) 604–611.
- [54] R. Sun, Q. Shi, M. Zhang, L. Xie, J. Chen, X. Yang, M. Chen, W. Zhao, *J. Alloy Compd.* 714 (2017) 619–626.
- [55] R. Amadelli, A. Molinari, I. Vitali, L. Samiolo, G.M. Mura, *Catal. Today* 101 (2005) 397–405.